Improving performance of reflectance diffuse optical imaging using a multicentered mode

Qing Zhao*
Lijun Ji*
Tianzi Jiang
Chinese Academy of Sciences
Institute of Automation
National Laboratory of Pattern Recognition
Beijing, China
E-mail: jiangtz@nlpr.ia.ac.cn

Abstract. We propose a novel multicentered mode for arrangement of optical fibers to improve the imaging performance of reflectance diffuse optical imaging (rDOI). Simulations performed using a semi-infinite model show that the proposed multicentered geometries can achieve a maximum of 42 overlapping measurements. The contrast-to-noise ratio (CNR) analysis indicates that the best spatial resolution is 1 mm in radius and the contrast resolution is less than 1.05 for the multicentered geometries. The results from simulations indicate significant improvement in image quality compared to the single-centered mode and previous geometries. Additional experimental results on a single human subject lead to the conclusion that the proposed multicentered geometries are appropriate for exploring activations in the human brain. From the results of this research, we conclude that the proposed multicentered mode could advance the performance of rDOI both in image quality and practical convenience.
[DOI: 10.1117/1.2400703]

Keywords: diffuse optical tomography; diffuse optical imaging; image quality; multicentered mode; optical fibers arrangement.

Paper 06012RR received Jan. 20, 2006; revised manuscript received Jul. 12, 2006; accepted for publication Jul. 18, 2006; published online Dec. 11, 2006.

1 Introduction

Diffuse optical imaging (DOI) is an appropriate tool for non-invasive exploration of hemoglobin concentration changes arising in biological tissues.[1–5] In the case of adult human brains,[6–9] reflectance DOI (rDOI) has been popularly applied because of the poor transparency of human brain tissues to near-infrared light. In rDOI, near-infrared light irradiates the brain tissues through optical fibers, and is received by detectors placed on the same surface as the sources. To date, the most widely used instruments for performing rDOI have been continuous-wave (CW) ones.[10–12] In CW instruments, the signal detected by one measurement may be influenced by absorption changes occurring in a large area, which was defined as the field of view (FOV) of the measurement. Hence the spatial resolution of rDOI has been limited. In addition, challenges occur in reconstructing high-quality images.

Numerous methods[13–17] have been developed to improve the image quality of DOI, of which enhancement of the overlapping measurement constituted an important group. Most researchers think that overlapping measurements are helpful for localizing the activations. In practice, such overlapping measurements were mainly obtained by the geometric arrangement of optical fibers. Several efforts have been made to improve the image quality through better arrangements of the optical fibers.[18–21] However, several challenges for the further improvement of the imaging performance of rDOI still exist for the following reasons.

1. It is difficult to add more sources and detectors into the previous geometries because of the limited dynamic ranges of the detectors. This limited further advancements in overlapping measurements.
2. In geometries used in rDOI to provide more overlapping measurements, the sources usually needed to be turned on set by set, so for some instruments the same task must be repeated several times to complete a single experiment. This made the rDOI experiments less convenient.

This work presents a multicentered mode for the arrangement of optical fibers. In this mode, several sources were located in the central area, and around these more detectors were placed. Significant improvements in overlapping measurements and image quality were shown by the results from simulations using a semi-infinite model. Experiments on a single human subject indicated that multicentered geometries are appropriate for probing human brains.

2 Arrangements

Single-centered and multicentered hexagonal geometries were evaluated in this study (Fig. 1). The sides of the equilateral hexagons were all 4 cm. The dots and open circles indicate the sources and detectors, respectively.

Figure 1(b) shows that the single-centered double-density (SD) geometry had 12 more detectors than the single-centered single-density (SS) geometry, which is shown in Fig. 1(a).

*Qing Zhao and Lijun Ji contributed equally to this work.
Address all correspondence to Tianzi Jiang, Chinese Academy of Sciences, Institute of Automation, National Laboratory of Pattern Recognition, 95 Zhongguancun East Road, Hai Dian District, Beijing, Beijing 100080 China; Tel: +86-10-82614469; Fax: +86-10-62551993; E-mail: jiangtz@nlpr.ia.ac.cn

1083-3668/2006/11(6)/064019/8/$22.00 © 2006 SPIE

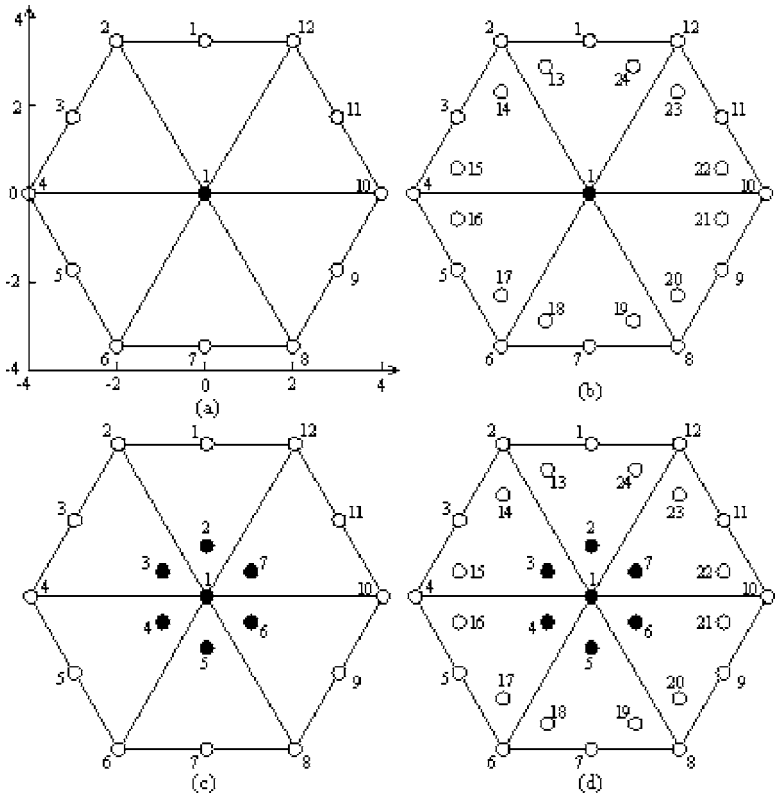

Fig. 1 (a) Single-centered single-density (SS) geometry, (b) single-centered double-density (SD) geometry, (c) multicentered single-density (MS) geometry, and (d) multicentered double-density (MD) geometry. The sources and detectors are indicated by dots and open circles, respectively.

Detector 13 in the SD geometry was located 5.8 mm below the top edge and was equidistant from detectors 1 and 2. The other 11 detectors were similarly located.

The multicentered geometries included multicentered single-density (MS) and multicentered double-density geometries (MD). They were formed by adding six more sources to the SS and SD geometries, respectively. As shown in Figs. 1(c) and 1(d), sources 2 were located on the lines defined by sources 1 and detectors 1, and were 1.15 cm away from the centers of the hexagons. The other five sources were placed in the same way.

In the MD geometry, the required dynamic ranges for every detector shown in Table 1 were all within the 60-dB dynamic range of our CW5 instrument (TechEn, Milford, MA). In the proposed geometries, each detector could receive signals from all of the sources, so the measurements achieved in the four geometries were SS - 12, SD - 24, MS - 84, and MD - 168. The imaging regions of the four geometries were the regions covered by the hexagons, and the pixel sizes were 1×1 mm.

Table 1 The maximal to minimal separation ratios, and the required dynamic ranges to maintain an SNR of 100 for every detector in the proposed MD geometry.

Detector number	Maximal separation (cm)	Minimal separation (cm)	Max/min ratio	Signal decrease (dB)	Required dynamic range (dB)
1,3,5,7, 9,11	4.62	2.31	2.00	23.79	43.79
2,4,6,8, 10,12	5.03	3.06	1.65	19.51	39.51
13 to 24	4.16	2.00	2.08	23.05	43.05

3 Theories

3.1 *Forward Model*

A semi-infinite model with an absorption coefficient of 0.1 cm^{-1} and a reduced scattering coefficient of 10 cm^{-1} was used in the simulations. The sources and detectors were placed on the air/tissue surface in the model, and the forward matrix $\boldsymbol{A}$ was calculated by the Rytov approximation.[22,23] Absorbers were located in the model. The referenced photon fluencies (Φ_0) were simulated in a semi-infinite model, and the measured photon fluencies (Φ) were calculated with absorbers located using the following equation:

$$\phi = \phi_0 \exp(\boldsymbol{A}^* \Delta\mu_a). \quad (1)$$

Here $\boldsymbol{A}$ is the forward matrix, and $\Delta\mu_a$ is the change in absorption coefficients after the absorbers are located. Gaussian noise was added to the simulated data to achieve an approximate signal to noise ratio (SNR) of 1000. Then, the changes in optical density (ΔOD) were calculated applying the following equation:

$$\Delta OD = -\ln(\phi/\phi_0). \quad (2)$$

Let y represent ΔOD and x represent the changes in absorption coefficient ($\Delta\mu_a$) at each pixel. We could rewrite the forward problem in the form $y=\boldsymbol{A}x$.

3.2 *Image Reconstruction*

The image of $\Delta\mu_a$ was reconstructed by the Tikhonov regularization method:[22–24]

$$\hat{x} = \boldsymbol{A}^T(\boldsymbol{A}\boldsymbol{A}^T + \alpha I)^{-1}y. \quad (3)$$

The parameter α in the equation was used to restrain the sensitivity of $\Delta\mu_a$ to the measurement noise. The noise in the simulated data was random, and hence, an L-curve method was performed to ascertain the best α for the reconstruction.[25–27]

4 Methods for Image Quality Evaluation

4.1 *Contrast-to-Noise Ratio Analysis*

The contrast-to-noise ratio (CNR) indicated whether the object could be clearly seen in the reconstructed image.[28,29] To calculate the CNR, the reconstructed image was divided into two parts, which were a region of interest (ROI) and a region of background (ROB). In the reconstructed image, the ROI was the region possessing the same location, shape, and size as the located object, while the ROB was defined as the residual. In this case, the mean values and variations of the reconstructed absorption coefficients over the ROI and ROB were calculated and the CNR was obtained by the equation:[29]

$$\mathrm{CNR} = \frac{\mu_{\mathrm{ROI}} - \mu_{\mathrm{ROB}}}{[w_{\mathrm{ROI}}\sigma^2_{\mathrm{ROI}} + w_{\mathrm{ROB}}\sigma^2_{\mathrm{ROB}}]^{1/2}}, \quad (4)$$

where w_{ROI} is the noise weight of the ROI, defined by dividing the area of the ROI by the area of the whole image, and $w_{\mathrm{ROB}}=1-w_{\mathrm{ROI}}\cdot\mu_{\mathrm{ROI}}$ and μ_{ROB} are the mean values of the objects and background regions in the reconstructed images, and σ_{ROI} and σ_{ROB} are the standard deviations.

4.2 *Shape Analysis*

The objects located in the model used in this work were all circular. However, the reconstructed objects were usually irregularly shaped. We believe that the regularity of the reconstructed objects served as another important criterion for judging the image quality. We defined the reconstructed objects as the pixels with values above the half maxima in the reconstructed images. The inscribed circles and the circumcircles of the reconstructed objects were then estimated. The circular ratio (CR) values were calculated with the following equation:

$$\mathrm{CR} = \frac{R_{\mathrm{ins}} - R_{\mathrm{cir}}}{R_{\mathrm{ins}}}, \quad (5)$$

where R_{ins} is the radius of the inscribed circles, and R_{cir} the radius of the circumcircles.

5 Simulation Results

In this section, we first compare the imaging performance of the multicentered geometries with the single-centered ones.

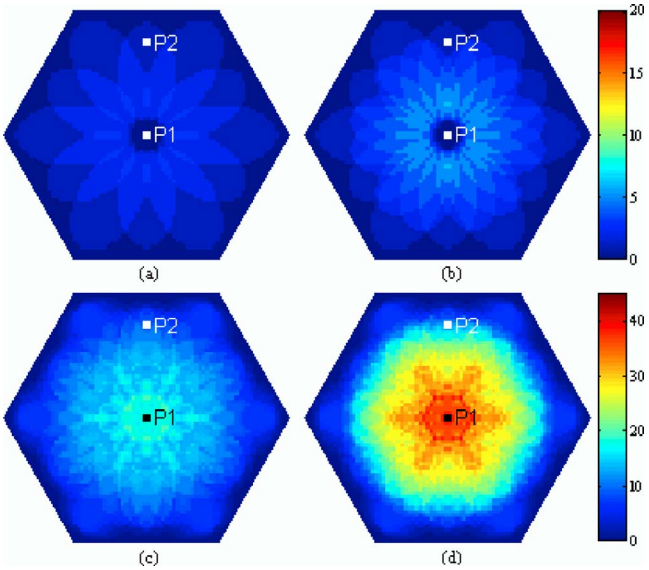

Fig. 2 Overlapping maps for the (a) SS, (b) SD, (c) MS, and (d) MD geometries.

Then, we show that our proposed multicentered geometries can achieve good image quality both in depths of 1.5 and 2.0 cm. Finally, we reveal the advancement in imaging performance by our multicentered geometries compared with previous geometries.

5.1 *Comparison of Multicentered Geometries to Single-Centered Ones*

5.1.1 *Improvement in overlapping measurements*

We monochromized the sensitivity matrix of the measurements at a depth of 1.5 cm with corresponding half-maxima. The number of overlapped FOVs at each pixel was counted afterward, and the achieved overlapping maps for the four geometries are shown in Fig. 2. The maximum overlapping measurements for the single-centered geometries were 3 and 6, while the multicentered ones were 19 and 42. The overlapping measurements in the center areas of the geometries were higher than those of the peripherals, as shown in Fig. 2. To fully evaluate the image quality of the geometries, we chose two positions: position 1 in the centers and position 2 in the peripheries. As seen in Fig. 2, the distances between all the positions 2 and the positions 1 were 25 mm.

The first four columns of Table 2 show the mean overlap-

Table 2 The first four columns show the mean overlapping measurements within 7.5 mm in radius around position 1 and position 2 for the four geometries. Columns five and six were obtained by dividing columns two and four by columns one and three, respectively. Columns seven and eight were the quotients obtained by dividing columns three and four by columns one and two, respectively.

	SS	SD	MS	MD	SD/SS	MD/MS	MS/SS	MD/SD
P1	1.29	3.07	17.20	35.51	2.38	2.06	13.33	11.57
P2	1.01	1.47	7.74	11.71	1.46	1.51	7.66	7.97

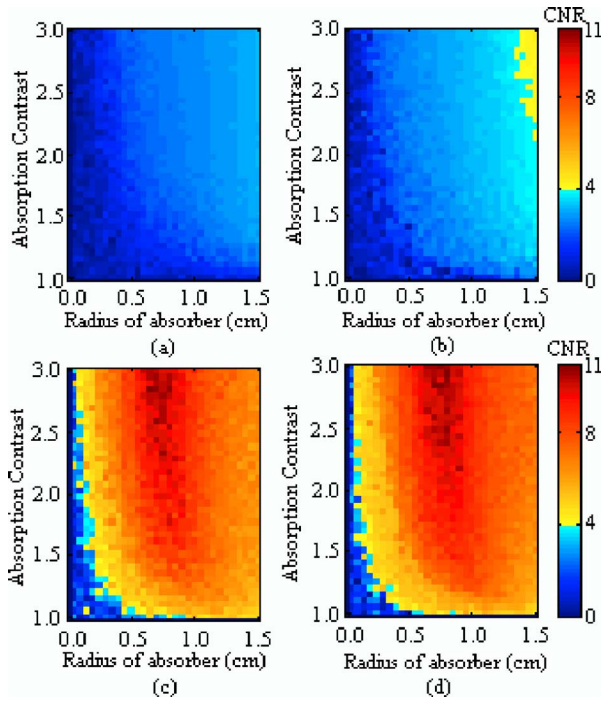

Fig. 3 CNR maps for the (a) SS, (b) SD, (c) MS, and (d) MD geometries in position 1.

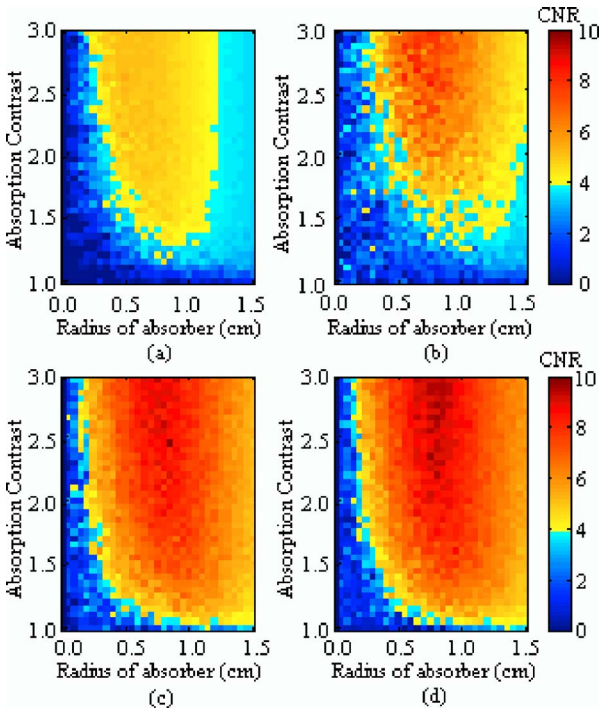

Fig. 4 CNR maps for the (a) SS, (b) SD, (c) MS, and (d) MD geometries in position 2.

ping measurements within 7.5 mm in the radius around each position 1 and position 2 for the four geometries. From columns five and six in Table 2, we can see the improvement in overlapping measurements provided by double-density geometries. Columns seven and eight show that multicentered geometries can increase the overlapping measurements even more significantly both in the center and periphery. Considering that the multicentered geometries had just six additional sources, it can be concluded that the multicentered mode is likely to effectively increase the overlapping measurements.

5.1.2 *Enhancement in image quality: a contrast-to-noise ratio analysis*

At each position proposed before, we changed the radii of the objects from 0.05 to 1.5 cm, and the contrast levels from 1.05 to 3.0. The intervals for the sizes and the contrast levels were 0.05 cm and 0.05, respectively. For each size and contrast level of the objects, imaging simulation was performed and the CNR value of the reconstructed image was calculated. The CNR maps of the four geometries for position 1 are shown in Fig. 3, followed by the CNR maps for position 2 in Fig. 4. The brighter areas indicating CNR values above 4.0 in the maps marked the objects that could be clearly recognized from reconstructed images. The threshold of 4.0 was chosen subjectively using the method suggested by Song et al.[29]

For these specified sizes and contrast levels of objects, larger CNR values were found in double-density geometries than in single-density ones, as shown in Figs. 3 and 4. Also, additional improvements could be observed in multicentered geometries than in single-centered ones, as seen in Figs. 3 and 4. This supports the conclusion that it was the multicentered mode, rather than the additional detectors, which was most effective in improving the image quality of rDOI.

Figures 3(c) and 3(d) show that the spatial resolutions were 1 mm and the contrast resolution limits were less than 1.05 for the multicentered geometries in position 1. Figures 4(c) and 4(d) reveal that the limits were 2 mm and 1.1 in position 2. As illustrated in Figs. 3(a) and 3(b) and Figs. 4(a) and 4(b), the single-centered geometries had higher spatial and contrast resolution limits in both positions.

5.1.3 *Enhancement in image quality: illustrational analysis*

We located objects with radii of 0.75 cm and contrast levels of 3.0 at a depth of 1.5 cm for the two positions. The real images are shown in Figs. 5(a) and 6(a). The radii of the inscribed circles and the circumcircles of the objects in Figs. 5(a) and 6(a) were 0.70 and 0.75 cm, respectively. The reconstructed images with the four geometries in position 1 are shown in Figs. 5(b)–5(e), followed by the reconstructed images in position 2 in Figs. 6(b)–6(e). The corresponding CNR and CR values of the reconstructed images are shown in Table 3.

In the case of objects located in position 1, only a few measurements could see the objects in single-centered geometries, [seen in Figs. 2(a) and 2(b) and Table 2], so the reconstructed images were very blurred [shown in Figs. 5(b) and 5(c)]. However, the multicentered geometries had many more overlapping measurements in position 1 [seen in Figs. 2(c) and 2(d) and Table 2], which helped to accurately ascertain the absorbers [shown in Figs. 5(d) and 5(e)]. And as a result, large CNR values were achieved.

In position 2, the objects detected by the single-centered

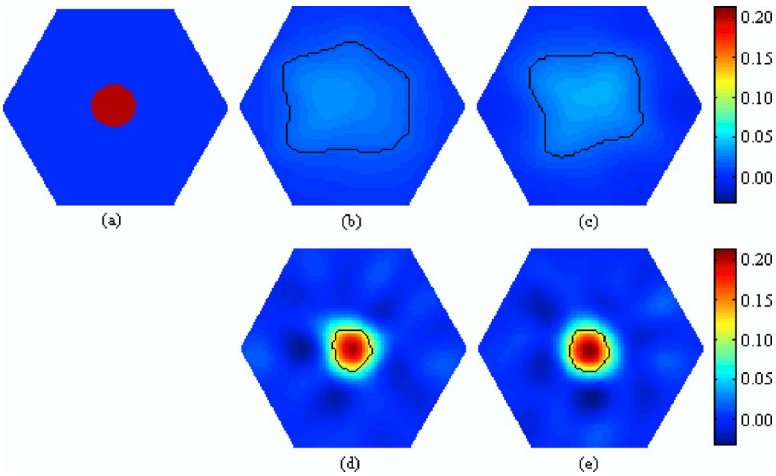

Fig. 5 The (a) true image and the reconstructed images using (b) SS, (c) SD, (d) MS, and (e) MD geometries in position 1. The objects were located 1.5 cm deep in a semi-infinite model. The black lines indicate the objects detected using the half-maximum method. The CNR and CR values are shown in Table 3.

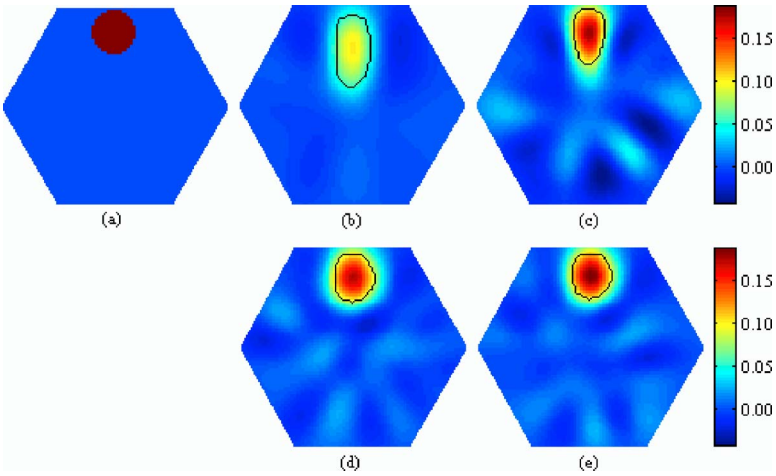

Fig. 6 The (a) true image and the reconstructed images with the (b) SS, (c) SD, (d) MS, and (e) MD geometries in position 2. The objects were located 1.5 cm deep in a semi-infinite model. The black lines indicate the objects detected using the half-maximum method. The CNR and CR values were shown in Table 3.

Table 3 The CNR and CR values of reconstructed images from the SS, SD, MS, MD, and rectangular geometries with objects located at 1.5 cm depth in a semi-infinite model.

	P1					P2				
Geometry	SS	SD	MS	MD	Rectangular	SS	SD	MS	MD	Rectangular
CNR	2.52	2.89	10.22	10.37	4.94	4.99	6.60	8.43	9.17	4.38
R_{ins} (cm)	1.70	1.60	0.70	0.70	0.85	0.65	0.55	0.75	0.75	1.20
R_{cir} (cm)	2.45	2.20	0.75	0.75	1.20	1.25	1.05	0.85	0.80	1.50
CR	0.44	0.38	0.07	0.07	0.41	0.92	0.91	0.13	0.07	0.25

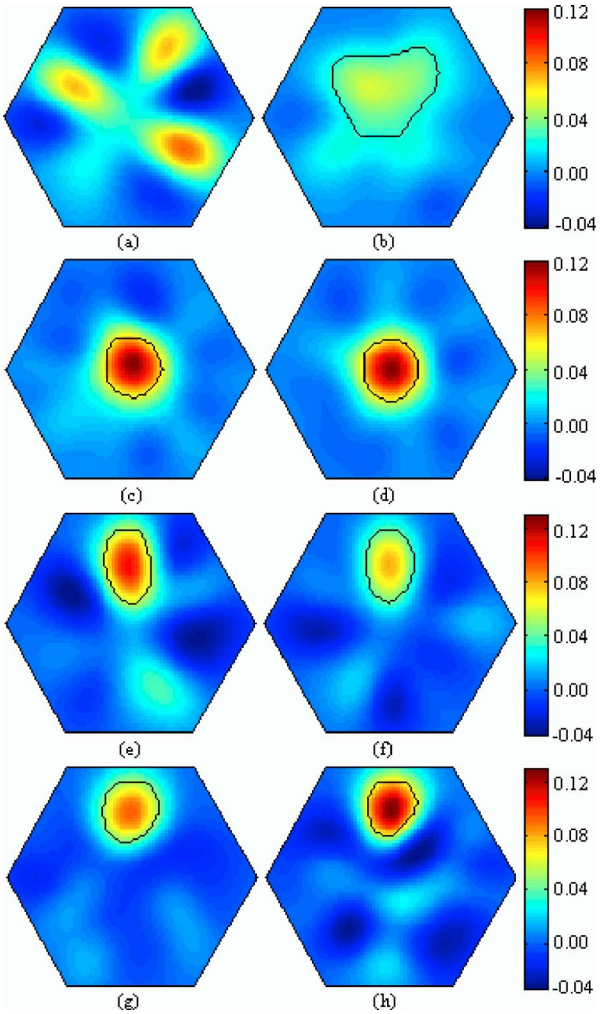

Fig. 7 Reconstructed images using the (a) SS, (b) SD, (c) MS, and (d) MD geometries in position 1. Also the reconstructed images using (e) SS, (f) SD, (g) MS, and (h) MD in position 2. The absorbers were located 2.0 cm deep in the semi-infinite model. The black lines indicate the objects detected using the half-maximum method. The CNR and CR values are shown in Table 4.

geometries were localized compared to the blurred objects in position 1, as shown in Figs. 6(b) and 6(c). However, the reconstructed objects were clearly oval shaped rather than circular and large CR values were obtained, as can be seen in Table 3. However, in the multicentered geometries, with increased densities of measurements [seen in Figs. 2(c) and 2(d) and Table 2], the shapes of the detected objects were clearly more nearly accurate [as in Figs. 6(d) and 6(e) and Table 3].

5.2 *Image Quality at Different Depths*

The absorbers were located 2.0 cm deep in the semi-infinite model. The reconstructed images for the four geometries are shown in Fig. 7. The corresponding CNR and CR values are shown in Table 4. A decrease in CNR values can be observed by comparing Table 3 with Table 4. The reconstructed images with the multicentered geometries were a little more blurred in Fig. 7 than those in Figs. 5 and 6. However, much better image quality could be obtained when comparing the reconstructed images with multicentered geometries to those with single-centered ones, as can be seen in Table 4 and Fig. 7. This indicated that the proposed multicentered geometries could achieve better image quality than single-centered ones both in depths of 1.5 and 2.0 cm.

5.3 *Comparing Multicentered Geometries to Previous Geometries*

To compare the image quality of the proposed multicentered geometries to previous ones done by other researchers, we compared ours with rectangular geometry, which has been demonstrated to have the best overlapping measurements and image quality of all the previously reported geometries used in rDOI.[21]

As seen in Fig. 8(b), rectangular geometry could achieve a maximum of nine overlapping measurements, and the mean overlapping measurements in positions 1 and 2 were 5.64 and 4.45, respectively. This indicates that the number of overlapping measurements in the rectangular geometry were much fewer than the number in our multicentered geometries. The reconstructed images from the rectangular geometry in Figs. 8(d) and 8(f) had smaller CNR values and larger CR values compared with those of multicentered geometries, as seen in Table 3. This also indicates that our multicentered geometries could achieve better image quality than rectangular geometry.

We reconstructed the images with the rectangular geometry and absorbers located 2.0 cm deep in the semi-infinite model. The corresponding CNR and CR values are shown in Table 4. Smaller CNR values and larger CR values can be found in Table 4 when comparing rectangular to multicen-

Table 4 The CNR and CR values of reconstructed images using the SS, SD, MS, MD, and rectangular geometries with objects located at 2.0 cm depth in a semi-infinite model.

	P1					P2				
Geometry	SS	SD	MS	MD	Rectangular	SS	SD	MS	MD	Rectangular
CNR	0.87	2.29	6.62	7.13	4.14	3.73	3.92	5.31	5.89	3.92
R_{ins}(cm)	—	1.15	0.90	0.90	1.20	0.75	0.80	0.90	0.80	1.30
R_{cir} (cm)	—	1.85	1.00	0.95	1.50	1.15	1.15	1.00	0.90	1.60
CR	—	0.61	0.11	0.06	0.25	0.53	0.44	0.11	0.13	0.23

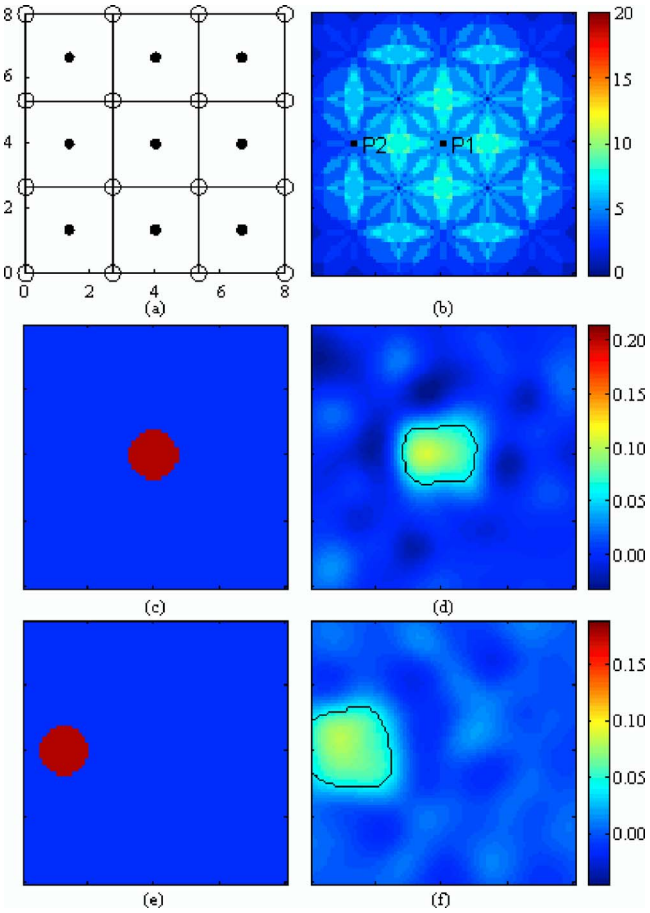

Fig. 8 The (a) rectangular geometry and its (b) overlapping map together with the real images in (c) position 1 and (e) position 2 and the reconstructed images in (d) position 1 and (f) position 2. The black lines in the reconstructed images indicate the objects detected using the half-maximum method. The CNR and CR values are shown in Table 3.

tered geometries. This indicates that the proposed multicentered geometries are better than rectangular geometry both in depths of 1.5 and 2.0 cm.

6 Preliminary Experimental Results

We confirmed our theoretical results by experiments using a CW5 instrument. Following a complete description of the experiments, written informed consent was obtained from a single human subject before the initiation of the experiments. These experiments were ethically approved by the Institutional Review Board at the Institute of Automation, Chinese Academy of Sciences. In the experiments, sources 1 in the multicentered and single-centered geometries were put on C3 in the EEG 10–20 system. The subject was asked to tap the right hand for 30 s, followed by 30 s of rest. Data collection lasted 420 s.

The data collected throughout the 420 s were averaged per minute to achieve averaged data for 60 s. The mean values of the first 30 s were viewed as Φ and those of the last 30 s were viewed as Φ_0. The images of $\Delta\mu_a$ were then reconstructed using Eqs. (2) and (3). As shown in Fig. 9, the reconstructed images with multicentered geometries were much clearer than

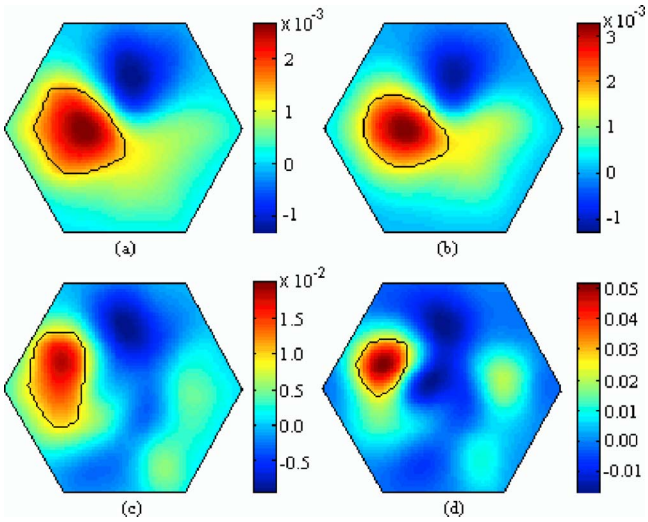

Fig. 9 Reconstructed images using the (a) SS, (b) SD, (c) MS, and (d) MD geometries from the experiments on a human subject.

those with the single-centered ones. As can be seen in Fig. 9, the areas of the reconstructed activations were 470 and 237 mm^2 from the MS and MD geometries.

During the experiments, the sources in the proposed multicentered geometries could be turned on simultaneously. As seen in Figs. 1(c) and 1(d), every detector would have no more than two measurements with separations shorter than 3.0 cm. Since the signals decreased rapidly for longer separations, the total power of the signals received by the detectors would be low. The lower signal power made it possible for the detectors to undergo amplification to maintain a good SNR.

Among the 168 measurements using the MD geometry, there were only three measurements that had an SNR of less than 100 during the experiments. When placed on a human head, the deformation of the multicentered geometries was small, and the optodes were able to contact tightly with the scalp, which also helped to achieve a good SNR.

7 Discussion

In rDOI, the quality of the reconstructed objects is primarily determined by the different types and degree of overlap of the measurements that are sensed by the absorbers. In locations with few overlapping measurements, absorbers with different shapes would influence the same or similar numbers of measurements. Since the overlapping areas of these measurements would remain unchanged, the reconstructed objects would appear to have the same shapes. However, using dozens of measurements sensitive to the objects, the image quality could become satisfactory in most cases.

The multicentered geometries were quite variable in practice. The distances from the centers to the sources and to the detectors were both alterable, and even the shape of hexagons could be easily changed to other polygons. The multicentered geometries that we propose were designed to be connected with each other to cover larger regions. After being linked, the image quality in the peripheral regions could be further improved.

In the MD geometry proposed, there were eight separations between sources and detectors: 2.0, 2.3, 3.1, 3.5, 4.0, 4.2, 4.6, and 5.0 cm. The multiseparations in the multicentered geometries are thought to be helpful for improving depth resolution.[15]

8 Conclusions

In this study, we propose a multicentered mode for the arrangement of optical fibers to improve the imaging performance of rDOI. The image quality and the practical performance of the multicentered geometries are evaluated. The results from the simulations show a significant enhancement in image quality compared with both single-centered and previous geometries. Preliminary experimental results on a human subject indicate that the proposed multicentered geometries are useful in practice for their good SNR and experimental convenience. In brief, the proposed multicentered geometries could advance the imaging performance of rDOI in both image quality and experimental performance.

Acknowledgments

The authors thank the reviewers for their constructive suggestions. They are also grateful to Rhoda E. and Edmund F. Perozzi, currently of Beijing University of Technology, for their extensive assistance with the English language. This work was partially supported by the Natural Science Foundation of China, grant numbers 30425004 and 60121302, and the National Key Basic Research and Development Program (973), grant number 2004CB318107.

References

1. S. Fantini, M. A. Fanceschini, and E. Gratton, "Non-invasive optical mapping of the piglet brain in real time," *Opt. Express* **4**, 308–314 (1999).
2. J. P. Culver, A. M. Siegel, J. J. Stott, and D. A. Boas, "Volumetric diffuse optical tomography of brain activity," *Opt. Lett.* **28**(21), 2061–2063 (2003).
3. S. Srinivasan, B. W. Pogue, S. Jiang, H. Dehghani, C. Kogel, S. Soho, J. J. Gibson, T. D. Tosteson, S. P. Poplack, and K. D. Paulsen, "Interpreting hemoglobin and water concentration, oxygen saturation, and scattering measured in vivo by nearinfrared breast tomography," *Proc. Natl. Acad. Sci. U.S.A.* **100**, 12349–12354 (2003).
4. E. Gratton, S. Fantini, M. A. Franceschini, G. Gratton, and M. Fabiani, "Measurements of scattering and absorption changes in muscle and brain," *Philos. Trans. R. Soc. London, Ser. B* **352**, 727–735 (1997).
5. J. C. Hebden, A. Gibson, R. M. Yusof, N. Everdell, E. M. Hillman, D. T. Delpy, S. R. Arridge, T. Austin, J. H. Meek, and J. S. Wyatt, "Three-dimensional optical tomography of the premature infant brain," *Phys. Med. Biol.* **47**(23), 4155–4166 (2002).
6. A. Maki, Y. Yamashita, Y. Ito, E. Watanabe, Y. Mayanagi, and H. Koizumi, "Spatial and temporal analysis of human motor activity using noninvasive NIR topography," *Med. Phys.* **22**, 1997–2005 (1995).
7. A. Villringer and B. Chance, "Non-invasive optical spectroscopy and imaging of human brain function," *Trends Neurosci.* **20**, 435–442 (1997).
8. H. Obrig and A. Villringer, "Beyond the visible—Imaging the human brain with light," *J. Cereb. Blood Flow Metab.* **23**, 1–18 (2003).
9. J. Choi, M. Wolf, V. Toronov, U. Wolf, C. Polzonetti, D. Hueber, L. P. Safonova, R. Gupta, A. Michalos, W. Mantulin, and E. Gratton, "Noninvasive determination of the optical properties of adult brain: near-infrared spectroscopy approach," *J. Biomed. Opt.* **9**(1), 221–229 (2004).
10. C. H. Schmitz, M. Löcker, J. M. Lasker, A. H. Hielscher, and R. L. Barbour, "Instrumentation for fast functional optical tomography," *Rev. Sci. Instrum.* **73**, 429–439 (2002).
11. A. Li, Q. Zhang, J. P. Culver, E. L. Miller, and D. A. Boas, "Reconstructing chromosphere concentration images directly by continuous-wave diffuse optical tomography," *Opt. Lett.* **29**(3), 256–258 (2004).
12. A. M. Siegel, J. J. A. Marota, and D. A. Boas, "Design and evaluation of a continuous-wave diffuse optical tomography system," *Opt. Express* **4**(8), 287–298 (1999).
13. A. Li, E. L. Miller, M. E. Kilmer, T. J. Brukilacchio, T. Chaves, J. Stott, Q. Zhang, T. Wu, M. Chorlton, R. H. Moore, D. B. Kopans, and D. A. Boas, "Tomographic optical breast imaging guided by three-dimensional mammography," *Appl. Opt.* **42**(25), 5181–5190 (2003).
14. B. W. Pogue and K. D. Paulsen, "High-resolution near-infrared tomographic imaging simulations of the rat cranium by use of *priori* magnetic resonance imaging structural information," *Opt. Lett.* **23**(21), 1716–1718 (1998).
15. D. A. Boas and A. M. Dale, "Simulation study of magnetic resonance imaging-guided cortically constrained diffuse optical tomography of human brain function," *Appl. Opt.* **44**(10), 1957–1968 (2005).
16. Y. Xu, H. L. Graber, Y. Pei, and R. L. Barbour, "Improved accuracy of reconstructed diffuse optical tomographic images by means of spatial deconvolution: two-dimensional quantitative characterization," *Appl. Opt.* **44**(11), 2115–2139 (2005).
17. M. A. Franceschini, V. Toronov, M. E. Filiaci, and E. Gratton, "Online optical imaging of the human brain with 160-ms temporal resolution," *Opt. Express* **6**, 49–57 (2000).
18. H. Xu, H. Dehghani, B. W. Pogue, R. Springett, K. D. Paulsen, and J. F. Dunn, "Near-infrared imaging in the small animal brain: optimization of fiber positions," *J. Biomed. Opt.* **8**(1), 102–110 (2003).
19. J. P. Culver, V. Ntziachristos, M. J. Holboke, and A. G. Yodh, "Optimization of optode arrangements for diffuse optical tomography: A singular-value analysis," *Opt. Lett.* **26**(10), 701–703 (2001).
20. T. Yamamoto, A. Maki, T. Kadoya, Y. Tanikawa, Y. Yamada, E. Okada, and H. Koizumi, "Arranging optical fibers for the spatial resolution improvement of topographical images," *Phys. Med. Biol.* **47**, 3429–3440 (2002).
21. D. A. Boas, K. Chen, D. Grebert, and M. A. Franceschini, "Improving the diffuse optical imaging spatial resolution of the cerebral hemodynamic response to brain activation in humans," *Opt. Lett.* **29**, 1506–1509 (2004).
22. S. R. Arridge, "Optical tomography in medical imaging," *Inverse Probl.* **15**, R41–R93 (1999).
23. D. A. Boas, A. M. Dale, and M. A. Franceschini, "Diffuse optical imaging of brain activation: approaches to optimizing image sensitivity, resolution, and accuracy," *Neuroimage* **23**, 275–288 (2004).
24. H. W. Engl, M. Hanke, and A. Neubauer, *Regularization of Inverse Problems*, Kluwer, Dordrecht (1996).
25. L. Wu, "A parameter choice method for Tikhonov regularization," *Electron. Trans. Numer. Anal.* **16**, 107–128 (2003).
26. P. C. Hansen and D. O'Leary, "The use of the L-curve in the regularization of discrete ill-posed problems," *SIAM J. Sci. Comput. (USA)* **14**, 1487–1503 (1993).
27. P. C. Hansen, "Regularization tools, a Matlab package for analysis and solution of discrete ill-posed problems," Version 3.0 for Matlab 5.2, Technical Report UNIC-92-03, Danish Computing Center for Research and Education, Technical University of Denmark (June 1992, revised June 1998), see http://www.netlib.org/numeralgo/na4. Version 2.1 for Matlab 4.2c, see http://www.netlib.org/numeralgo/na4-matlab4.
28. B. W. Pogue, C. Willscher, T. O. McBride, U. L. Osterberg, and K. D. Paulsen, "Contrast-detail analysis for detection and characterization with near-infrared diffuse tomography," *Med. Phys.* **27**(12), 2693–2700 (2000).
29. X. Song, B. W. Pogue, S. Jiang, M. M. Doyley, and H. Dehghani, "Automated region detection based on the contrast-to-noise ratio in near-infrared tomography," *Appl. Opt.* **43**(5), 1053–1062 (2004).